Journal of Mechanical Design. Received June 29, 2018;
Accepted manuscript posted January 05, 2019. doi:10.1115/1.4042624

CONTROL OF PROCESS SETTINGS FOR LARGE-SCALE ADDITIVE MANUFACTURING WITH SUSTAINABLE NATURAL COMPOSITES

Yadunund Vijay
Engineering Product Development
Singapore University of Technology and Design
Singapore, 487372

Naresh D. Sanandiya
Engineering Product Development
Singapore University of Technology and Design
Singapore, 487372

Stylianos Dritsas
Architecture and Sustainable Design
Singapore University of Technology and Design
Singapore, 487372

Javier G. Fernandez
Engineering Product Development
Singapore University of Technology and Design
Singapore, 487372

ABSTRACT

We present a system for 3D printing large-scale objects using natural bio-composite materials which comprises of a precision extruder mounted on an industrial six-axis robot. This paper highlights work on controlling process settings to print filaments of desired dimensions while constraining the operating point to a region of maximum tensile strength and minimum shrinkage. Response surface models relating the process settings to geometric and physical properties of extruded filaments, are obtained through Face-Centered Central Composite Designed experiments. Unlike traditional applications of this technique which identify a fixed operating point, the models are used to uncover dimensions of filaments obtainable within operating boundaries of our system. Process setting predictions are then made through multi-objective optimization of the models. An interesting outcome of this study is the ability to produce filaments of different shrinkage and tensile strength properties, by solely changing process settings. As a follow up, we identify optimal lateral overlap and inter-layer spacing parameters to define toolpaths to print structures. If unoptimized, the material's anisotropic shrinkage and non-linear compression characteristics cause severe delamination, cross-sectional tapering and warpage. Lastly, we show the linear scalability of the shrinkage model in 3D space which allows for suitable toolpath compensation to improve dimensional accuracy of printed artefacts. We believe this first ever study on the parametrization of large-scale additive manufacture technique with bio-composites will serve as reference for future sustainable developments in manufacturing.

1 INTRODUCTION

While advances have been made to increase the rate and scale of additive manufacturing, the concept of doing so sustainably has long been overlooked. Solutions that achieve desirable rates and scales, either employ thermoplastics (ABS, PLA, PU Foam) [1-3] which are not naturally compostable [4, 5], cementitious materials [6, 7] with limited recyclability [8], or use technologies that require special chemical environments [9]. Composites of natural materials with good mechanical properties provide enhanced sustainability benefits. However, their unmodified use in additive manufacturing is limited as they are often mixed with plastics or hazardous solvents and in general their use has been demonstrated only on smaller scales [10-13].

The material used in this study originates in prior work [14]. It is a cellulosic-chitinous composite completely bio-sourced and biodegradable outside composting facilities. In its cured state, its mechanical properties are similar to commercial rigid polyurethane foams (pcf-30), while in its wet state, it exhibits thixotropy and it is highly pliable. Hardening occurs naturally overtime at ambient conditions. The additive manufacturing method used is classified as Material Extrusion [15]. It resembles the Direct Ink Writing [16] method given use of a wet colloid which does not require phase transition to 3D print. However, as in a Fused Deposition Modelling process, a filamentary layered assembly approach is employed. With the extruder mounted on an industrial robot, the scale of the process extends to the physical reach of the robot.

Printing large-scale artifacts that faithfully embody the design geometry requires control of the geometry of extruded material filaments individually and assemblies thereof into layers. Achieving control requires understanding material behavior during fabrication and identifying suitable settings for key process parameters. Unlike well characterized industrial materials, use of natural composites for additive manufacturing inherently increases process complexity as a result of the innate variability in material properties. Similar to other bio-composites employed in sustainable manufacturing [10, 13, 17, 18], our material is water based. This introduces challenges as hardening by removal of embodied moisture, results into significant dimensional and structural changes. The material employed has a dynamic viscosity of 1,500 Pa.s, determined as optimal for extrusion [14]. Given its pliability, the geometry of filaments is highly dependent on several process parameters. Further, the dimensions of layers change dynamically as layers are added and from shrinkage during the drying phase.

With lack of theoretical modelling explaining these complex phenomena, to overcome challenges and enable printing,

Journal of Mechanical Design. Received June 29, 2018;
Accepted manuscript posted January 05, 2019. doi:10.1115/1.4042624

development of experimental models offers an alternative approach. Predictive models relating geometric properties of deposited filaments to process parameters have been developed for other additive manufacturing processes including parametric fitting based on geometric assumptions of filament profiles [19], non-parametric model fitting using complex algorithms [20, 21] and finite element analysis [22]. Across those, datasets are generated from large number of experiments with various combinations of process parameters values. Harvesting large amounts of data in this manner is often time and resource intensive.

In this paper, we rely on efficient data sampling and statistical analysis to derive empirical models relating significant process parameters to the dimensions (widths and heights at wet and dry states) and tensile strengths of filaments. Selected parameters include the robot's linear velocity at the end-effector (v_R), material flow rate through the nozzle (f_M) and the vertical offset between nozzle and print surface (z_N). The composition of the material including its viscosity was held constant as per optimized results obtained in prior work [14]. While other factors such as temperature and humidity do affect the process, their effects are ignored in the study given the inability to vary them in the environment of the system. Derived models by designed experiments are used to forward map process parameters to achievable filament properties within the constraints of the manufacturing process. Inverse model interrogation enables predicting values for process parameters such that desirable dimensions of filaments can be printed while ensuring operating points where shrinkage is retained at minimum and tensile strength at maximum.

The paper is organized in the study of Primary Effects: pertaining material extrusion settings including motion speed, flow rate and layer offset to achieve controllable filament properties, presented in Section 3.1; and Secondary Effects**:** pertaining additive assembly of filaments, further disaggregated into adjacent filament adhesions to achieve fusion and prevent delamination in plane, presented in Section 3.2; and vertical layer compaction to achieve predictable geometric features of filament stacks, presented in Section 3.3. Lastly, combination of those studies is used to inform printing strategies for manufacturing large-scale prototypes. As the primary effects are in the critical path to accessing secondary, the bulk of this paper focuses on those.

2 MATERIALS AND METHODS

2.1 Manufacturing System Design

The additive manufacturing system consists of three main components: a six-axis articulated industrial robot, a precision material dispenser and a material pump system [Figure 1]. The robot has a maximum horizontal reach of 1.65m and a payload capacity of 20kg at its flange. It is mounted on a purpose-built hydraulic scissor lift platform which extends its overall reach to 3.7m vertically and indefinitely horizontally. The precision dispensing unit mounted at the flange has a maximum flowrate of 2.8ml/s. The unit is driven by a motor whose speed is set from the robot's controller. The dispensed material flows out of a custom designed nozzle with internal diameter of 7mm. Material is transported to the flange via a stainless steel braided hose from the commercial bulk unloading pump system. The entire system is capable of transporting highly viscous materials (max 2,000 Pa.s) and it is rated for 2MPa pressure. The pump and dispenser use anti-sheer and anti-pulsation eccentric screw drives. Parametric software for motion planning and code generation of controlled material extrusion along algorithmically generated toolpaths was developed using the Jeneratiff digital fabrication library [23] within the Rhinoceros/Grasshopper environment.

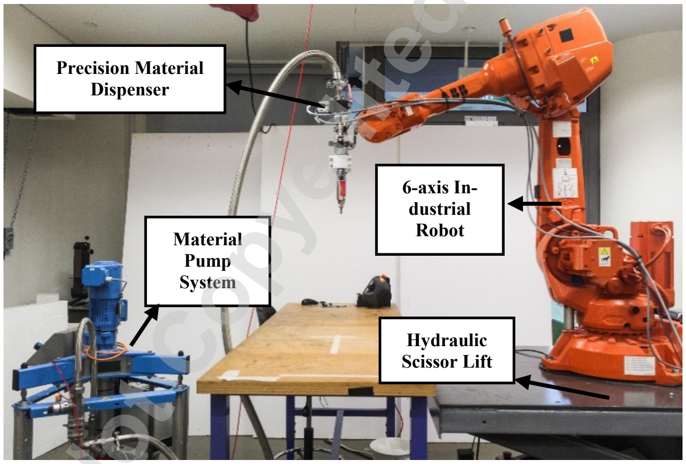

FIGURE 1. ADDITIVE MANUFACTURING SYSTEM OVERVIEW

2.2 Design of Experiment Methodology

Any manufacturing process may be black-boxed to a set of controllable and un-controllable factors that operate on raw material to bring about a change in its geometry or material properties [24]. In processes with multiple controllable factors, the effect of varying one on the measurable outputs (responses) may not be apparent. Then, estimating the net effect of changing several factors becomes non-trivial. Departing from a trial and error approach, the Design of Experiment methodology delineates techniques for efficient data sampling, and statistical evaluations to identify significant factors and the effects of their interactions on the response of interest [25]. In its simplest form, a 2^k Factorial Experiment for 'k' controllable factors, is one where 2 levels (High, Low) are assigned to each factor. Then all combinations of factor levels are experimentally investigated through trials. From the responses measured, the E*ffects* of each factor combination, which is the change in response produced by a change in the level of the factor combination, can be calculated and the significance determined through an analysis of variance (ANOVA) [25, 26]. The ANOVA method partitions the total variability in the dataset (Total Sum of Squares) into variations from factors & combinations (Factor Sum of Squares) and an error term (Error Sum of Squares). The Mean Squared Errors for each term is then computed followed by a test statistic that follows the F-distribution. If the calculated F-Value exceeds the tabular value at an appropriate significance level, the factor combination is treated as significant. Alternatively, if the P-Value statistic for the factor is lower than the significance level (typically 0.05), the factor or combination term is statistically significant [25]. Linear regression models relating significant controllable factors to responses

Journal of Mechanical Design. Received June 29, 2018;
Accepted manuscript posted January 05, 2019. doi:10.1115/1.4042624
Copyright © 2019 by ASME

can then be derived and analyzed to predict operating points that achieve desirable outputs. The various regression coefficients can be directly estimated from the previously computed *Effects* terms [27, 28]. However, non-linear effects of factors may be significant thereby rendering simple linear models ineffective at describing the process. More extensive experiment designs to fit higher order models may be required [29]. The need for such models can be statistically evaluated by measuring responses at factor levels equal to the mean of their High and Low levels (Center level), followed by the evaluation of a Curvature statistic [25]. This statistic is computed using Eqn. 1 where n_F, n_C, $\bar{y}_F$ & $\bar{y}_C$ are the number for factorial & center points and mean of factorial & center points respectively. The significance of the Curvature term is then determined by estimating its F-Value or P-Value term.

$$SS_{Curvature} = \frac{n_F * n_C(\bar{y}_F - \bar{y}_C)^2}{n_F + n_C} \tag{1}$$

Higher order models can be fit from experiment data generated from combinations of factors at three different levels [25]. However, this approach requires 3^k experiment runs which can be time consuming and expensive. Instead of designing a new experiment, the Response Surface Methodology [30] provides a solution to generate second order response surface models by appending the data collected from the Factorial and Center point runs. The Full Factorial design can be transformed to a Central Composite one by the addition of Axial points. With the extra data points, the *Effects* of quadratic terms can be computed as with the linear terms, following which their regression coefficients can be estimated. Such designs allow for relatively efficient fitting of second order models to the responses [25]. The quadratic models can then be evaluated to find optimal process setting to achieve desired performance [31-33].

In this study, the Design of Experiment methodology is not used to find a single optimal operating point, rather its process modelling efficiency is exploited to map values of adjustable process parameters to the output of the process. The parameters identified are robot linear velocity at the end-effector (v_R), material flow rate through the nozzle (f_M) and the vertical offset between nozzle and print surface (z_N). The desired geometric properties we aim to control with these factors are the initial width (W_i) and height (H_i) of wet filaments, the final width (W_f) and height (H_f) of filaments after drying and the tensile strength (T_f) of dry filaments. The approach adopted attempted to fit linear models relating controllable parameters to responses through a 2^3 Full Factorial experiment with design space as seen in Figure 2. Then, through evaluation of the Curvature statistic, determine whether higher order models are required and if so, employ Central Composite Design methodology to derive higher-order models.

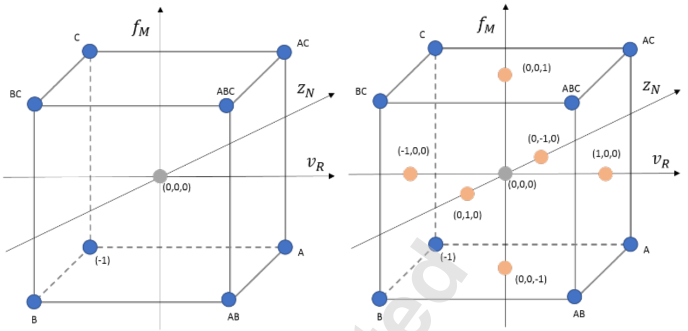

FIGURE 2. LEFT: DESIGN SPACE OF 2^3 FULL FACTORIAL EXPERIMENT, RIGHT: DESIGN SPACE OF 2^3 FACE-CENTERED CENTRAL COMPOSITE DESIGN EXPERIMENT. THE BLUE, GREY AND ORANGE POINTS CORRESPOND TO THE FACTORIAL, CENTER AND FACE-CENTERED EXPERIMENT POINTS RESPECTIVELY.

2.3 Metrology and Data Analysis

Considering the pliability of the material, we deploy optical systems to measure the dimensions of prints in wet state. Two cameras (Canon 650D with EOS 18-55 lenses) were used to capture the top view and side view of filaments. Each camera was calibrated such that its focal plane was coincident with the top and side-planes of the filaments respectively. A gauge of known dimensions included in the field of view served as a reference for the conversion of distances between pixels to distances in SI units. The optical measurement setup achieves a measurement resolution of $50\mu m$.

As the edges of printed filaments are not smooth, point-to-point measurement were avoided. Instead, localized bounding boxes were drawn at three zones on the images as seen in Figure 3 and the heights were averaged. The zones are located away from the filament extremities which are influenced by start-stop motion of the extruder. When drawing bounding boxes, care is taken to ensure that the lengths average out the surface irregularities. The technique is sufficiently accurate as irregularities are under $200\mu m$ while the dimensions of interest are in several millimeters.

The width of a filament is measured from the top-view image, while the height from the side-view image. Measurements of filaments in wet and dry states were made using the same technique. An Instron 5943 system with a 1kN load cell was employed to measure the tensile stress of printed filaments as well as the maximum shear force required to separate overlapping filaments. ImageJ software was used to measure dimensions from images. Minitab 18 software was utilized to compute ANOVA tables, fit regression models and perform multi-objective optimization.

Journal of Mechanical Design. Received June 29, 2018;
Accepted manuscript posted January 05, 2019. doi:10.1115/1.4042624

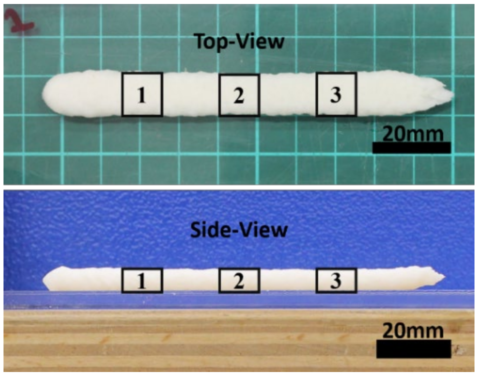

FIGURE 3. ZONES FOR DIMENSIONAL MEASUREMENT OF FILAMENTS

3 PROCESS DEVELOPMENT AND OPTIMIZATION

3.1 Extrusion Process Model

The geometry of extruded filaments is highly dependent on the controllable machine settings [Figure 4]. Initially, to derive linear models relating the controllable factors to the desired responses, a 2^3 Full-factorial experiment with 2 corner point replicates and 6 center point replicates was performed. The *low, center* and *high-level* values for the three factors [Table 1] were selected with the aim of maximizing the experimental design space while ensuring feasibility of all experimental runs. The Full Factorial experiment runs along with associated process settings are listed in Table 3. For each run, the responses are measured as described in Section 2.3. A visualization of a subset of the generated dataset is seen in Figure 4.

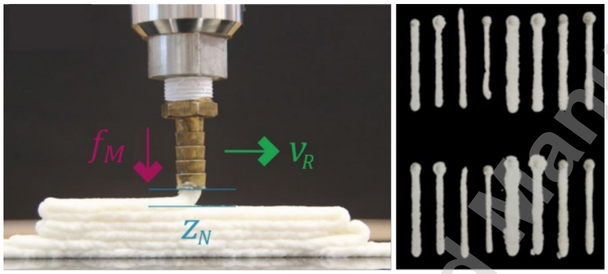

FIGURE 4. LEFT: PROCESS PARAMETERS USED IN THE STUDY. RIGHT: SUBSET OF GENERATED DATASET

TABLE 1. DECODED VALUES OF CONTROLLABLE FACTORS

Controllable Parameters	Actual Levels			Coded Levels		
	Low	Center	High	Low	Center	High
v_R	40mm/s	50mm/s	60mm/s	-1	0	1
z_N	3.50mm	5.25mm	7.00mm			
f_M	1.49ml/s	2.05ml/s	2.61ml/s			

The dataset was analyzed for all the responses and the *Effects* of various terms including the Curvature were evaluated. Table 2 presents the ANOVA for the wet width (W_i) response. The Degrees of Freedom (DF), Adjusted Sum of Squares (Adj SS), Adjusted Mean Squares (Adj MS), F-Value and P-Value terms are presented for all the factors and their combinations. The presence of curvature in the model is highly significant as indicated by small P-Value (<0.05) of the Curvature Source. This Curvature term, measures the deviation of center point measurements from the expected center point of a cube formed by the 2^3 design space [25]. The significance of curvature also arises in ANOVA of other responses. These observations confirm the insufficiency of fitting linear models to the responses.

TABLE 2. ANOVA OF 2^3 FULL FACTORIAL EXPERIMENT WITH CENTER POINTS FOR RESPONSE W_i

Source	DF	Adj SS	Adj MS	F-Value	P-Value
Model	8	128.75	16.09	1464.36	0.00
Linear	3	110.96	36.99	3365.35	0.00
v_R	1	31.51	31.51	2867.06	0.00
z_N	1	38.30	38.30	3484.52	0.00
f_M	1	41.15	41.15	3744.46	0.00
2-Way Interactions	3	11.12	3.71	337.25	0.00
$v_R * z_N$	1	3.12	3.12	283.46	0.00
$v_R * f_M$	1	2.39	2.39	217.20	0.00
$z_N * f_M$	1	5.62	5.62	511.08	0.00
3-Way Interactions	1	0.02	0.02	1.54	0.24
$v_R * z_N * f_M$	1	0.02	0.02	1.54	0.24
Curvature	**1**	**6.66**	**6.66**	**605.59**	**0.00**
Error	13	0.14	0.01		
Total	21	128.89			

To overcome the significant curvature, modifications were made to the experiment to sample additional points to fit higher order models. The experiment was transformed to a Face-Centered Central Composite Design by the inclusion of 6 additional axial runs with an Axial Spacing (α) of 1 [Figure 2] and responses for the axial runs were measured.

The dataset with axial runs [Table 3] was then analyzed to fit higher order models. For each response, only significant quadratic terms as indicated by their P-Values were included in the respective surface models. Higher order terms were added until the Lack-of-Fit statistic was insignificant (P-Value>0.05). The ANOVA for W_i response following the inclusion of higher order terms is presented in Table 4. The overall *Regression* is significant (P-Value<0.05) while the *Lack-of-Fit* is insignificant (P-Value>0.05). The fitted model has an *Adjusted* R^2 of 99.72%. These statistics validate the appropriateness of our model and similar approaches for model fitting were followed for the other responses.

Journal of Mechanical Design. Received June 29, 2018;
Accepted manuscript posted January 05, 2019. doi:10.1115/1.4042624
Copyright © 2019 by ASME

TABLE 3. MEASURED VALUES OF RESPONSES FROM DIFFERENT EXPERIMENT RUNS

Point Location	v_R	z_N	f_M	W_i		H_i		W_f		H_f		T_f	
				R1	**R2**	**R1**	**R2**	**R1**	**R2**	**R1**	**R2**	**R1**	**R2**
Corner (Facto-rial)	-1	-1	-1	10.43	10.38	3.05	3.04	9.09	8.98	2.47	2.36	4.92	4.90
	1	-1	-1	7.36	7.49	3.12	3.01	6.03	6.02	2.41	2.40	5.38	4.46
	-1	1	-1	7.50	7.60	5.16	5.16	5.40	5.43	4.28	4.33	4.29	3.83
	1	1	-1	6.50	6.43	4.97	4.95	5.19	4.86	4.37	4.22	0.10	0.00
	-1	-1	1	15.29	15.72	3.38	3.32	13.93	14.09	2.68	2.66	3.43	3.22
	1	-1	1	11.14	11.08	3.28	3.40	9.40	9.06	2.52	2.46	4.81	5.17
	-1	1	1	10.39	10.43	5.85	5.98	8.52	8.24	4.96	4.98	2.93	2.78
	1	1	1	7.57	7.72	5.28	5.14	5.73	5.74	4.33	4.35	3.89	4.54
Centre	0	0	0	8.25	8.27	4.99	4.94	7.02	6.69	3.73	3.64	4.60	5.41
	0	0	0	8.37	8.35	4.96	4.97	6.96	6.71	3.69	3.55	5.00	4.92
	0	0	0	8.31	8.42	4.93	4.94	6.80	6.70	3.67	3.66	4.56	5.09
Axial	-1	0	0	10.22	10.08	4.57	4.51	8.33	8.36	4.00	3.86	3.69	4.32
	1	0	0	7.49	7.53	4.63	4.67	5.52	5.51	3.74	3.85	4.74	4.74
	0	-1	0	11.01	11.34	3.48	3.46	9.92	9.97	2.57	2.53	4.60	5.58
	0	1	0	7.63	7.54	5.43	5.37	6.08	6.01	4.62	4.35	4.45	4.45
	0	0	-1	6.67	6.86	4.58	4.63	5.33	5.16	3.69	3.58	4.77	4.03
	0	0	1	9.59	9.55	4.98	4.87	8.07	8.43	3.62	3.65	3.79	3.83

TABLE 4. ANOVA OF CENTRAL COMPOSITE DESIGNED EXPERIMENT FOR RESPONSE W_i.

Source	DF	Adj SS	Adj MS	F-Value	P-Value
Regression	11	160.86	14.62	1127.36	0.00
v_R	1	38.45	38.45	2964.01	0.00
z_N	1	12.91	12.91	995.42	0.00
f_M	1	7.88	7.88	607.28	0.00
$v_R * v_R$	1	1.04	1.04	80.12	0.00
$z_N * z_N$	1	5.25	5.25	404.51	0.00
$f_M * f_M$	1	0.27	0.27	20.69	0.00
$v_R * z_N$	1	3.12	3.12	240.16	0.00
$v_R * f_M$	1	2.39	2.39	184.02	0.00
$z_N * f_M$	1	5.62	5.62	433.02	0.00
$v_R * v_R * z_N$	1	0.20	0.20	15.37	0.00
$v_R * v_R * f_M$	1	0.13	0.13	9.91	0.01
Error	22	0.29	0.01		
Lack-of-Fit	**3**	**0.06**	**0.02**	**1.56**	**0.23**
Pure Error	19	0.23	0.01		
Total	33	161.14			

The resulting surface models for all the responses are as seen through Eqn. 2- 6. The constant term in the models is the value of the response (in mm or MPa) we expect if the machine parameters are set to their Centre-point values. The coefficient of each term represents the change in response value we can expect from a unit change of the corresponding variable (in dimensionless coded values). Tensile strength (T_f) response was transformed by square root operation to overcome diverging spread of residuals at fitted values. A discussion on the residuals from the data fitting experiment can be found in Annex A.

$$\begin{aligned} W_i = {} & 8.364 - 1.3866 v_R - 1.797 z_N + 1.403 f_M + 0.440 v_R^2 + \\ & 0.990 z_N^2 - 0.224 f_M^2 + 0.441 v_R z_N - 0.386 v_R f_M - \\ & 0.592 z_N f_M + 0.250 v_R^2 z_N + 0.200 v_R^2 f_M \end{aligned} \tag{2}$$

$$\begin{aligned} H_i = {} & 4.872 + 0.056 v_R + 0.966 z_N + 0.159 f_M - 0.214 v_R^2 - \\ & 0.374 z_N^2 - 0.044 f_M^2 - 0.116 v_R z_N - 0.067 v_R f_M + \\ & 0.054 z_N f_M + 0.089 v_R^2 z_N + 0.038 v_R^2 f_M - \\ & 0.169 v_R z_N^2 - 0.0598 v_R z_N f_M \end{aligned} \tag{3}$$

$$\begin{aligned} W_f = {} & 6.856 - 1.366 v_R - 1.949 z_N + 1.486 f_M + 0.042 v_R^2 + \\ & 1.108 z_N^2 - 0.140 f_M^2 + 0.595 v_R z_N - 0.502 v_R f_M - \\ & 0.564 z_N f_M + 0.231 v_R^2 z_N - 0.060 v_R z_N f_M \end{aligned} \tag{4}$$

$$\begin{aligned} H_f = {} & 3.705 - 0.096 v_R + 0.987 z_N + 0.119 v_R^2 - 0.222 z_N^2 - \\ & 0.107 f_M^2 - 0.056 v_R z_N - 0.099 v_R f_M + 0.047 z_N f_M + \\ & 0.131 v_R^2 f_M - 0.057 v_R z_N f_M \end{aligned} \tag{5}$$

$$\begin{aligned} \sqrt{T}_f = {} & 2.184 + 0.092 v_R - 0.091 z_N - 0.075 f_M - 0.059 v_R^2 + \\ & 0.027 z_N^2 - 0.133 f_M^2 - 0.0130 v_R z_N + 0.103 v_R f_M + \\ & 0.017 z_N f_M \end{aligned} \tag{6}$$

$$v_R, z_N, f_M \ \epsilon \ [-1,1]^R$$

Surface plots as seen through Figures 5-9 provide a visualization of the values of responses in the process space described by Eqn. 2- 6. The contour plots as seen in Figure 10 provide an estimate of achievable build rates. The minimum and maximum

Journal of Mechanical Design. Received June 29, 2018;
Accepted manuscript posted January 05, 2019. doi:10.1115/1.4042624

values for each response along with corresponding machine settings to produce respective responses are presented in Table 5. It is noteworthy that wider and narrower filaments than the nozzle diameter (7mm) can be produced as seen in the experiment data in Table 3 and predicted ranges in Table 5. However, in practice, printing multiple layers with too large or narrow widths leads to severe cross-sectional wall tapering and buckling, respectively.

Visualization of achievable cross-sectional filament areas is presented in Figure 10. An unexpected behavior captured by the model is the ability to vary cross-sectional areas despite keeping material flow rate constant. This phenomenon perhaps arises due to process-induced effects that operate on the soft material used. For example, printing at higher motion speeds tends to stretch filaments along their length, while smaller nozzle offsets tend to flatten filaments during deposition. Combinations of those parameters perhaps modify internal material compaction and hence result into filaments with varying densities and strengths. The models also highlight avenues for increasing build rate which is presently limited by the flow rate (f_M), provided a higher pressure material unloading system than the one in current use.

TABLE 5. PREDICTED RANGES OF RESPONSES ALONG WITH MACHINE SETTINGS TO ACHIEVE THE SAME

Response	Range		Min. Settings (coded)			Max. Settings (coded)		
	Min (l)	Max (u)	v_R	z_N	f_M	v_R	z_N	f_M
W_i (mm)	5.91	15.53	1	0.252	-1	-1	-1	1
H_i (mm)	3.03	5.90	-1	-1	-1	-1	1	1
W_f (mm)	4.35	14.04	1	0.232	-1	-1	-1	1
H_f(mm)	2.34	4.97	0.172	-1	1	-1	1	1
T_F(MPa)	2.84	5.51	1	1	-1	0.879	-1	-0.010

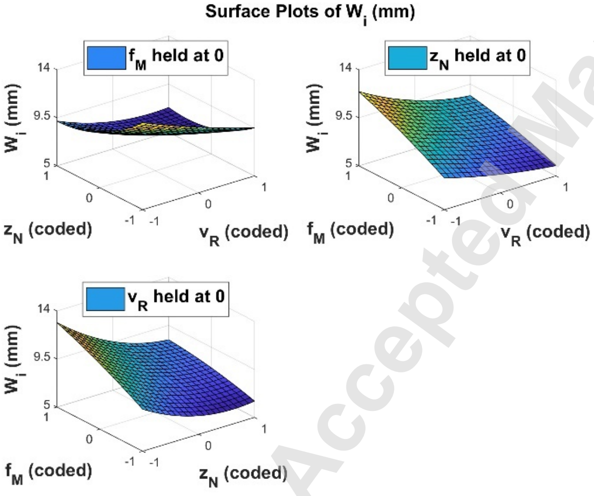

FIGURE 5. SURFACE PLOTS OF WIDTH OF FILAMENTS IN WET STATE

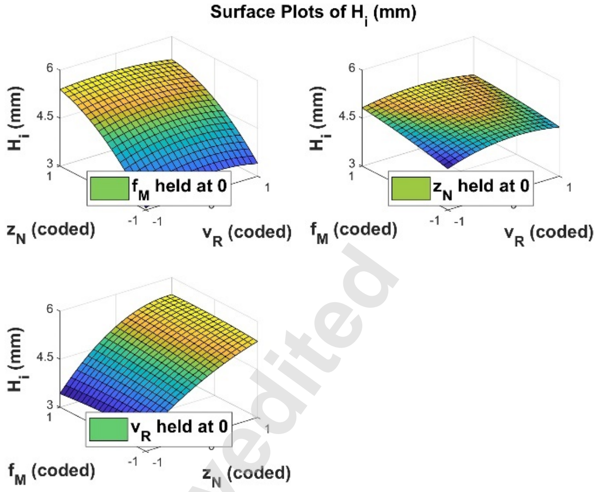

FIGURE 6. SURFACE PLOTS OF HEIGHT OF FILAMENTS IN WET STATE

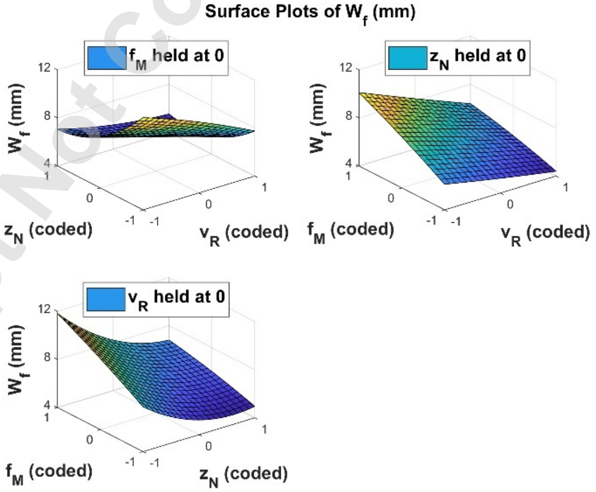

FIGURE 7. SURFACE PLOTS OF WIDTH OF FILAMENTS IN DRY STATE

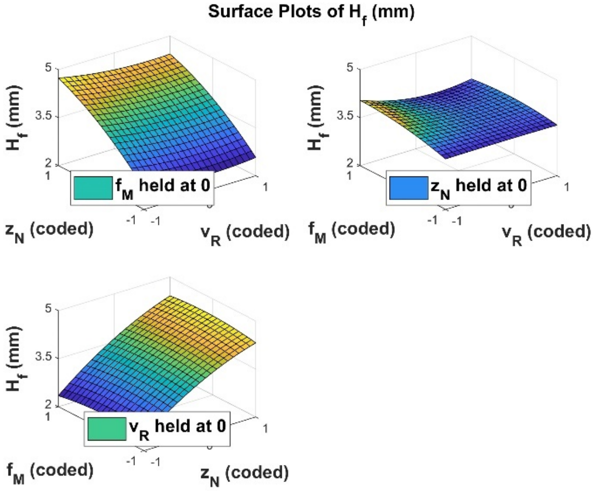

FIGURE 8. SURFACE PLOTS OF HEIGHT OF FILAMENTS IN DRY STATE

Journal of Mechanical Design. Received June 29, 2018;
Accepted manuscript posted January 05, 2019. doi:10.1115/1.4042624

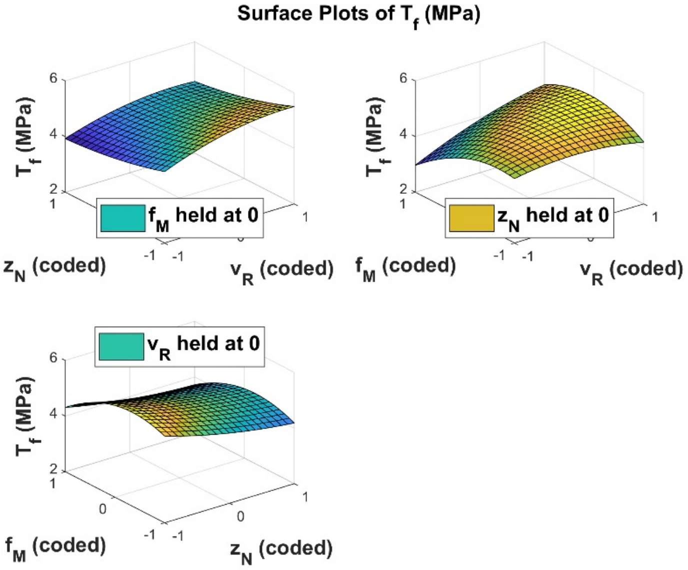

FIGURE 9. SURFACE PLOTS OF TENSILE STRENGTH OF PRINTED FILAMENTS AS FUNCTION OF PROCESS SETTINGS

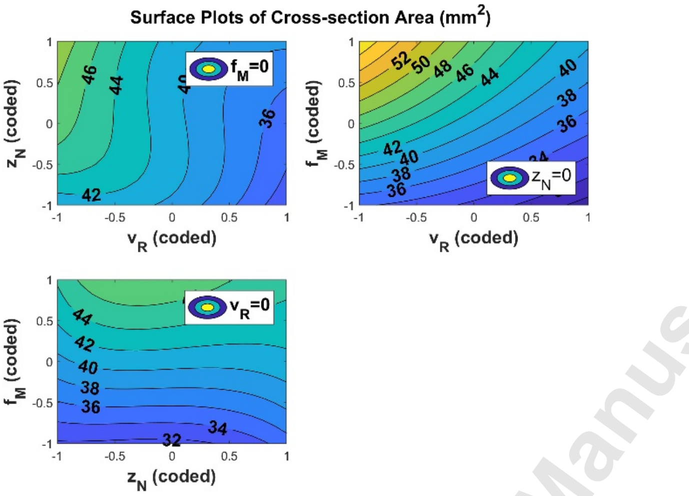

FIGURE 10. CONTOUR PLOT OF CROSS-SECTIONAL AREA OF FILAMENT IN WET STATE

3.1.1 Multi-objective Optimization.

Minitab's multi-optimization framework is used to predict values of the machine settings to produce filaments of desired properties. Each response (y_i) is assigned a *desirability function* ($d_i = F(y_i)$) based on the required constraint for the response [34]. The range of these functions is zero to one where one represents the most desirable outcome. A *Composite Desirability (D)* is defined as the geometric mean of the individual desirability functions. The solver aims to identify set of values for independent variables such that the Composite Desirability function is maximized. For example, if it is desired to print a filament of specific width and height, responses W_i & H_i are assigned Target desirability functions as seen in Eqn 7 [34]. Here y is the fitted regression equation, l & u are the lower and upper limits (Table 5), t is the target value and w is a Weight parameter for the response respectively. As per requirements, other responses may assigned Target, Maximize or Minimize desirability functions.

$$\begin{array}{cc} \textit{if Target} & \textit{if Maximize} \\ d = \begin{cases} 0, & y \le l \\ \left(\dfrac{y-l}{t-l}\right)^{w}, & l < y \le t \\ \left(\dfrac{y-u}{t-u}\right)^{w}, & t < y \le u \\ 0, & y > u \end{cases} & = \begin{cases} 0, & y \le l \\ \left(\dfrac{y-l}{u-l}\right)^{w}, & l < y \le u \\ 1, & y > u \end{cases} \end{array} \tag{7}$$

The optimization problem is then as presented below. Weight parameters in the individual desirability functions may be adjusted appropriately if the error between converged and desired solutions is significant for responses of importance.

$$\begin{gathered} \mathit{maximize}\ D = \left(\prod_{i=1}^{5} d_i\right)^{\frac{1}{5}} \\ \mathit{subject\ to,} \\ v_R, z_N, f_m \,\epsilon\, [-1,1]^R \\ y_i \epsilon\, [l_i, u_i]^R \\ d_i > 0 \end{gathered} \tag{8}$$

Figure 11 highlights the results obtained from the optimization of responses to print a filament of wet width and height of 12mm and 4mm respectively while minimizing shrinkage (by maximizing dry dimensions) and maximizing tensile stress. For the specified constraints, the optimal values of the controllable factors (x, in coded units) are presented along the current value at the top of the figure.

In this optimization, W_i & H_i responses were assigned Weight parameters of 10 & 2 respectively while Weights for the other responses were set to 1 each. This was done to maximize individual desirability functions of W_i & H_i as the priority is to achieve dimensional control of filaments. The coefficients for these responses were manually incremented from the base value of 1, until the error between their individual Desirability and Target values were below the optical measurement resolution of $50\mu m$. The line plots in the figure show how the Composite Desirability and responses change as a function of the controllable factor listed in the respective column footer, while other factors are held constant at their current values. The trade-off for achieving dimensional control is evident from the high individual desirability values for W_i & H_i but lower Composite Desirability. This is a result of weighting other responses lower, which allows for less favorable values of their individual desirability functions.

Upon conversion of the coded numbers to absolute values, we concluded that printing with the robot speed set to 49mm/s, nozzle offset at 3.98mm from the baseplate and material extrusion rate set to 2.43ml/s, can produce filaments with the predefined properties. In *Results and Discussions*, we discuss the accuracy of our models by comparing measured data to expected values.

Journal of Mechanical Design. Received June 29, 2018;
Accepted manuscript posted January 05, 2019. doi:10.1115/1.4042624

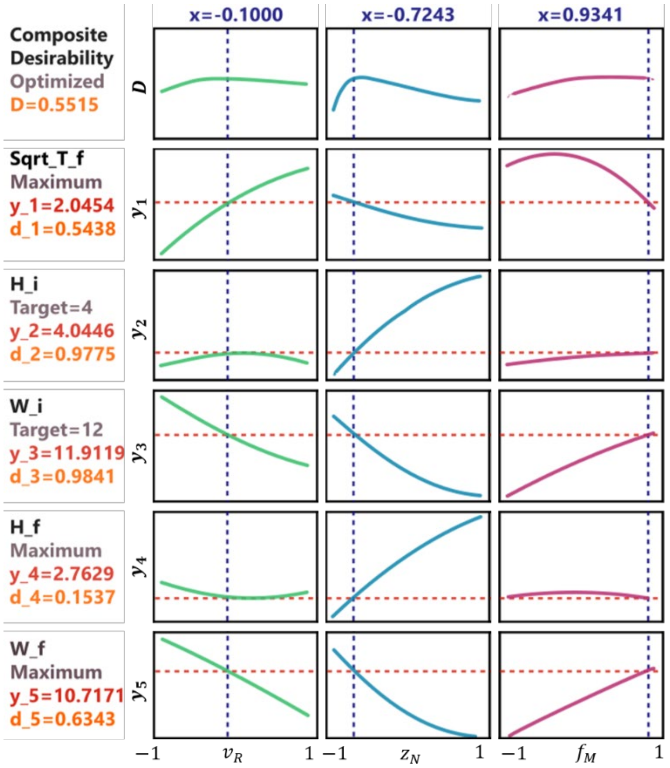

FIGURE 11. RESULTS OF MULTI-OBJECTIVE OPTIMIZATION TO PREDICT PROCESS SETTINGS FOR DESIRED DIMENSIONAL AND PHYSICAL PROPERTIES OF SINGLE FILAMENTS

3.2 Planar Parameter Evaluation

3.2.1 Lateral Overlap

Adjacent filaments of the material can form as a homogenous solid body provided there is sufficient fusion between the two. Weakly fused filaments will shrink away from one another creating a crevice in between and can even separate completely. The pliability of the material can be exploited to improve fusion. A filament can be printed adjacent to another with overlap if the toolpaths of the filaments are spaced nearer than the width of an individual filament in the same plane. In this situation, the momentum from the material extrusion for printing the second filament pushes material into the first, causing compaction of the first while enhancing fusion of the two filaments. If the overlap is too large, it will cause undesired displacement of deposited material. Also, while larger overlaps might result in greater bond strengths, they would also increase the overall toolpath distance required to fill the same space with material. Hence, it is desirable to identify an optimal lateral overlap.

An experiment was conducted to determine the optimal lateral overlap between two filaments such that a strong bond is achieved post drying without delamination. For 12mm wide filaments of height 4mm, samples were printed with lateral overlap values ranging from 2mm to 6mm in steps of 0.5mm. The process settings to print filaments of desired dimensions were derived from multi-objective optimization of the response surface models.

FIGURE 12. LEFT: TEST SET OF VARYING LATERLAP OVERLAP DISTANCE. RIGHT: MEASUREMENT OF SHEAR FORCE USING INSTRON

Three replicates at each overlap level were printed and tested. The length of the bonded region (bond length) was held constant at 42mm for all samples, which was assumed to be the minimum overlap any toolpath would include [Figure 12]. After oven drying the samples at $50°C$ for 24h, the maximum shear force of the joints was measured by pulling filaments apart along their lengths using a tensile tester (Instron 5943). The results of the experiment are presented in Figure 13.

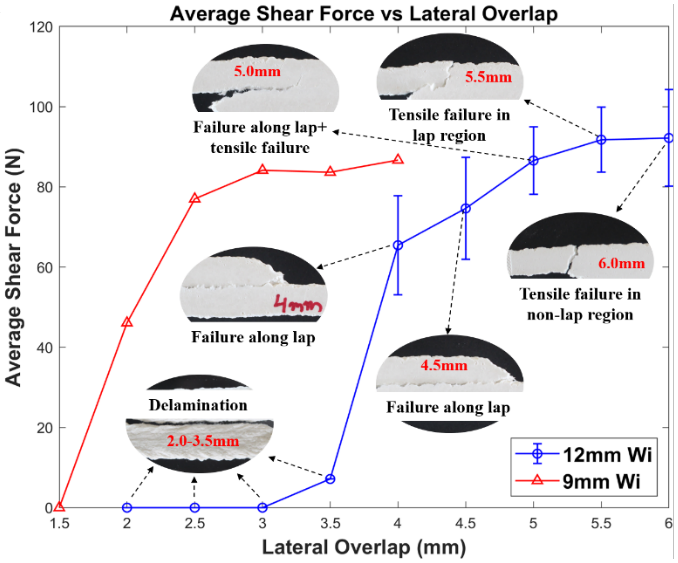

FIGURE 13. GRAPH OF AVERAGE SHEAR FORCE REQUIRED TO SEPARATE LATERALLY OVERLAPPING FILAMENTS

Journal of Mechanical Design. Received June 29, 2018;
Accepted manuscript posted January 05, 2019. doi:10.1115/1.4042624
Copyright © 2019 by ASME

The data points with zero shear force reading correspond to instances where the overlap distance was insufficient and led to separation of the filaments upon drying. As seen in the graph, for both filament types, the strength of the bond increases with the lateral overlap distance. However, beyond a threshold, the strength of the combined unit saturates resulting in the non-overlapping region failing in tension before the shearing of the bonded filaments. The experiment was repeated with filaments of 9mm width & 4mm height, and a similar trend was observed [Figure 13].

3.2.2 Planar Scaling of Shrinkage

Filaments printed with material employed in this study shrink anisotropically as they transition from wet to dry state. For 100mm long, 12mm wide and 4mm thick filaments printed along the direction of their lengths with settings derived previously, we observe 5mm (5%), 1.4mm (12%) and 1.3mm (32%) reduction in length, width and height respectively. The directional dependency of the shrinkage results from the different stresses experienced by the material (pulling along the length, compression along height) which are process induced and not its natural tendency. We sought to understand if shrinkage of overlapping filaments conformed to any linear relationship to the number of such overlapping units. We printed overlapping filaments with the introduction of voids to form repeating square units. The lateral overlap distance was held constant at 6mm while the number of repeating units were increased [Figure 14].

The overall dimensions of filamentary units were measured at the time of printing and after drying. From the measurements, the dimensional loss due to shrinkage is calculated. While the shrinkages along the length and thickness dimensions were as in the case of a single filament, the shrinkage of the overall widths shows a linear relationship to the number of repeating units as seen in the graph in Figure 15.

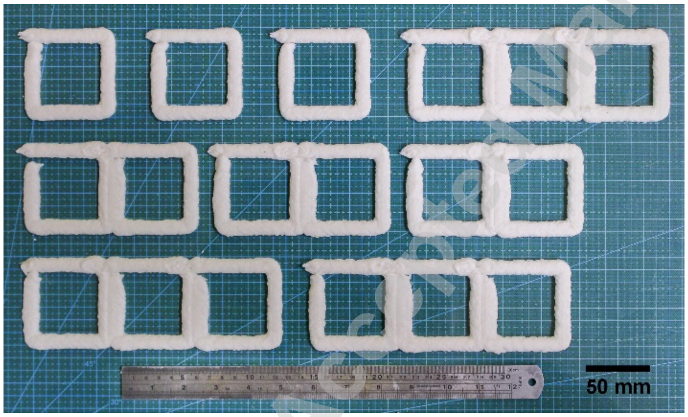

FIGURE 14. REPEATING OVERLAPPING SQUARE UNITS OF EDGE LENGTH 60MM

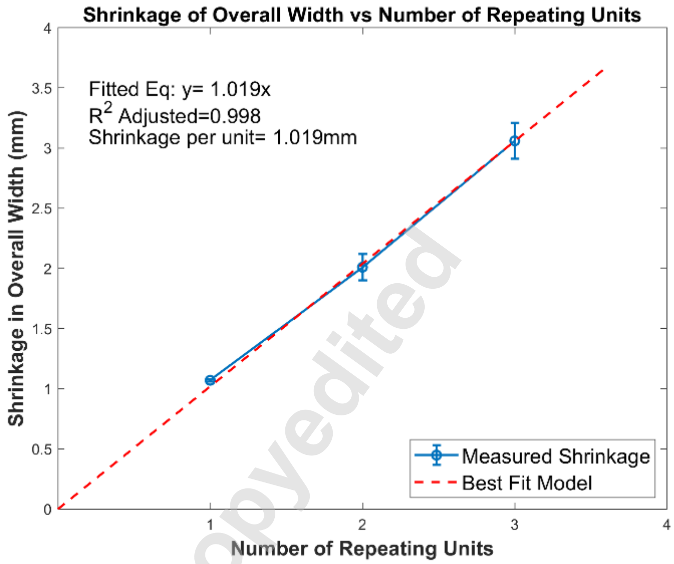

FIGURE 15. GRAPH OF SHRINKAGE IN OVERALL WIDTH AS A FUNCTION OF NUMBER OF REPEATING UNITS

3.3 Vertical Parameter Evaluation

3.3.1 Layer Spacing Effects

A common strategy to 3D print an object is to contour it into layers of constant spacing along the vertical axis, and then starting from the bottommost layer, deposit material to fill up space within the contour boundary. The constant spacing parameter is often equal to the height of the solidified layer underneath as in the case of FDM, SLS, DED, Binderjet and Polyjet processes [35]. The dimensions of a solidified layer in these processes remains constant as layers are added above. However, in our process, there is a dynamic change in the width and height of extruded filaments as layers of wet material are added. The change is attributed to three factors: 1) Variable Substrate Stiffness which is the variation in stiffness of print surface, 2) Momentum of Material Jet which is momentum of extruded material and 3) compression due to Self-Weight.

For the same process settings, when material is deposited on printed layers and not on the baseplate, the new filaments tends to be narrower and thicker than expected. This is because the stiffness of the wet composite underneath is several orders of magnitude lower than the baseplate which results in inadequate spreading of newly deposited material. For the first printed layer, the stiffness of the baseplate causes the material jet to spread out upon impact to achieve filaments wider than the nozzle diameter. While layers printed on material are narrower and thicker, they eventually flatten out to some extent when layers are printed above it. This flattening occurs due to momentum of the material extruded for printing layers above as well as the weight of added layers.

Journal of Mechanical Design. Received June 29, 2018;
Accepted manuscript posted January 05, 2019. doi:10.1115/1.4042624

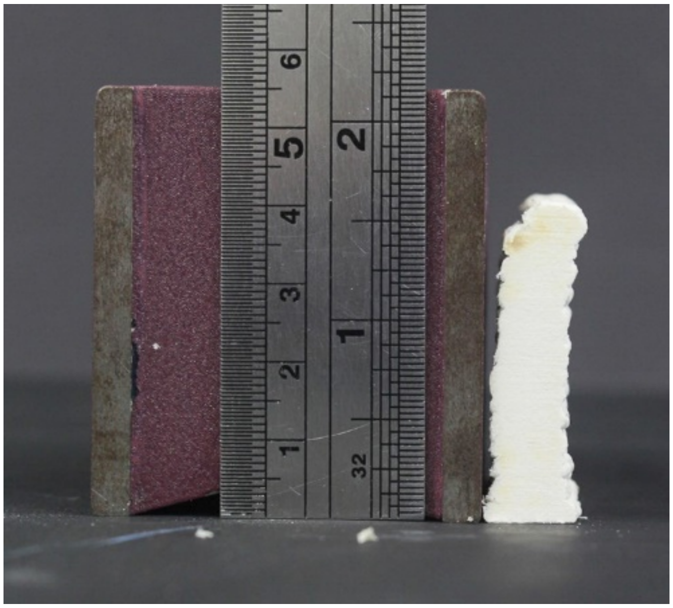

FIGURE 16. TAPERING OF CROSS-SECTION OF 13 VERTICALLY STACKED FILAMENTS LEADING TO BUCKLING

These effects cause tapering of cross-section of printed walls which worsens the dimensional accuracy of prints and more concerningly allows for fewer stackable layers before collapse [Figure 16]. To quantify the dimensional change, 100mm x 12mm x 4mm filaments were printed one above another and the dimensions of each layer was recorded before and after the addition of another layer. The contour distance between the layers was set to 4mm- the expected height per layer. During deposition, the Nozzle Offset from the contour level was 3.98mm as predicted from the multi-objective optimization. Figure 17 & 18 present graphs that track the width and height of a given layer as additional layers are printed above. They also track the width and height of the topmost layer as a function of number of layers.

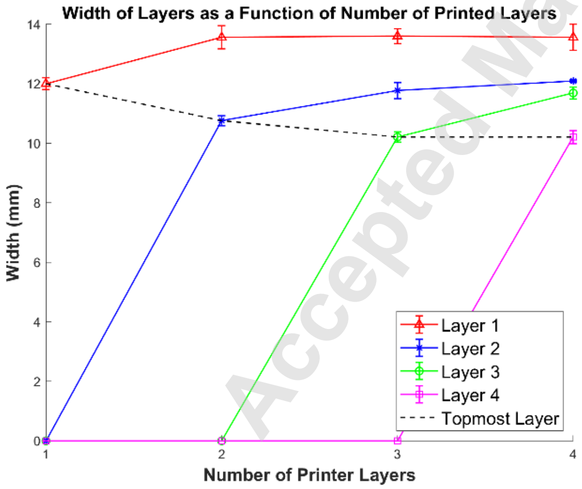

FIGURE 17. TRACKING CHANGES IN WIDTH OF PRINTED LAYERS AS LAYERS ARE ADDED ABOVE

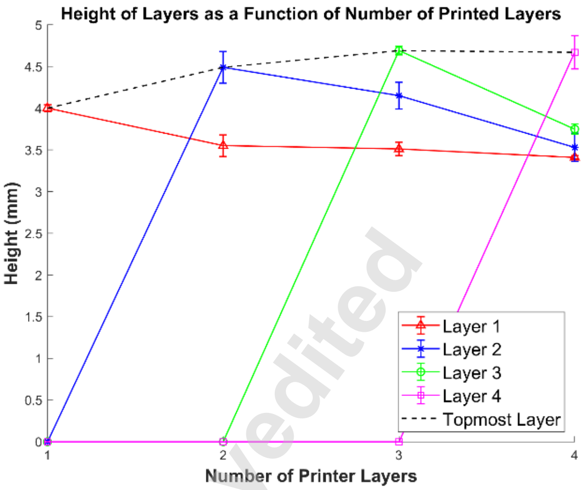

FIGURE 18. TRACKING CHANGES IN HEIGHT OF PRINTED LAYERS AS LAYERS ARE ADDED ABOVE

3.3.2 Vertical Scaling of Shrinkage

As discussed, a variety of effects lead to compression of the height of printed layers in the wet state. Further reduction in height of layers is observed post-drying due to shrinkage. To quantify the overall reduction in height, various cylinders with different number of layers were printed with the process settings that produce 12mm wide and 4mm thick filaments. The contour spacing between the layers was set to 3mm to alleviate tapering as discussed in Section 4.3. Once dry, the heights of the cylinders were measured, and the results are presented in the Figure 19.

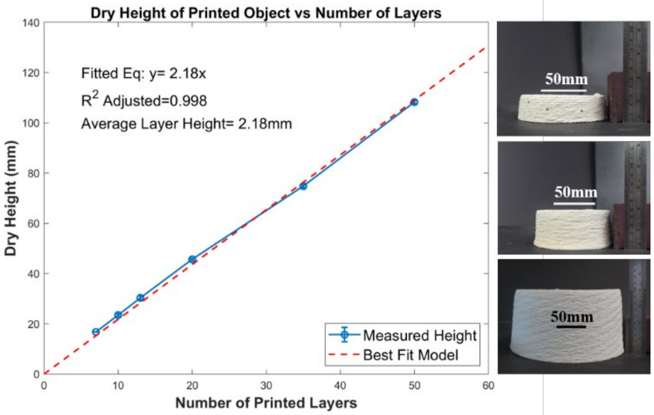

FIGURE 19. GRAPH OF DRY HEIGHTS OF PRINTED CYLINDERS AS A FUNCTION OF NUMBER OF PRINTED LAYERS

4 RESULTS AND DISCUSSIONS

4.1 Accuracy of Extrusion Models

To test the accuracy of our fitted models, we printed 3 replicates of filaments with two different predicted settings respectively. The first set of settings were those presented in Section 3.1.1. The second set of settings of $v_R = 41mm/s, z_N = 4.58m$ & $f_M = 1.69ml/s$ were obtained from multi-objective

Journal of Mechanical Design. Received June 29, 2018;
Accepted manuscript posted January 05, 2019. doi:10.1115/1.4042624

optimization to print wet filaments of 9mm width and 4mm thickness while minimizing shrinkage and maximizing tensile strength.

The width and height of all filaments in wet and dry states were measured along with their tensile strengths upon drying. The results are summarized in Table 6. Overall, these results affirm the accuracy of our models and our approach.

FIGURE 20. FILAMENTS PRINTED WITH FIRST SETTINGS AS OBTAINED FROM MULTI-OBJECTIVE OPTIMIZATION

TABLE 6. COMPARISON OF PREDICTED RESPONSE VALUES AGAINST MEASURED VALUES

Desired Wet State Geometry	Response Variables	Predicted Response	Avg. Measured Response	Abs. % Error
12mm Width, 4mm Height	$W_i\ (mm)$	11.91	12.07	1%
	$H_i\ (mm)$	4.04	3.91	3%
	$W_f\ (mm)$	10.72	10.60	1%
	$H_f\ (mm)$	2.76	2.74	1%
	$T_f\ (MPa)$	4.18	4.13	1%
9mm Width, 4mm Height	$W_i\ (mm)$	9.00	8.92	1%
	$H_i\ (mm)$	4.00	4.14	3%
	$W_f\ (mm)$	7.36	7.40	1%
	$H_f\ (mm)$	3.26	3.46	6%
	$T_f\ (MPa)$	4.58	4.51	2%

4.2 Planar Experiment Results

For both the 9mm and 12mm wide filaments, there exists a critical overlap distance (3.5mm and 5mm respectively) beyond which the strength of the bonded region is greater than that of a single filament. This result has a significant implication. It indicates that despite the material's high viscosity, individual filaments can homogenize provided a threshold level of mixing is induced during deposition. This re-affirms the material's applicability in a process like additive manufacturing where adjacent filaments of material need to be fused together to create objects. A generalized rule of thumb for determining lateral overlap distance can be stated based on the results- *For filaments of width* X*, an overlap of* $0.4X$ *produces strong joints without delamination upon drying*. A thorough evaluation of this empirical rule is left open for future work.

The linear scaling of shrinkage of overall width along with constant shrinkage in length and height of the repeating units provides valuable insights on developing pathing algorithms which predict and suitably compensate for shrinkage.

4.3 Vertical Experiment Results

The results of the experiment described in Section 3.3.1 yield multiple interesting insights on the material behavior which allow us to alleviate tapering and improve height accuracy of prints. First, we see that the material undergoes non-linear compression as the changes in dimensions do not scale linearly with applied loading. Instead, the widths and heights of filaments tend to saturate at certain values. This is suggestive of a localized zonal effect of loading. In other words, the compression characteristics of a given layer is only significantly affected by a limited 'k' layers above it. Another insight is the saturation of substrate stiffness as indicated by plateauing measures of width and height of the topmost filament printed. This allows us to extend this 'k-neighbor' theory whereby the final dimensions of a given layer are only affected by 'k' layers above and below the given layer.

Seeing how the height of layers saturates around 3mm, the spacing between contours was modified from 4mm to 3mm with aims of improving overall accuracy of contour levels. To validate the improvement, a 19-layer wall, with toolpaths spaced 3mm apart vertically, was printed with the same machine settings. As evident in Figure 21, the printed wall is significantly free of cross-sectional taper as compared to the previously un-optimized conditions. Interestingly, although the Optimized Wall contains 6 additional layers than the Un-optimized Wall, it exhibits greater stability given its uniform cross-sectional area. Under the optimized condition, the width and height of the wet layers was measured to be 13.3mm and 3mm respectively while the same when dry were 12mm and 2.3mm. The shrinkage in width dimension is exactly as predicted from our shrinkage model for a single filament.

The results of experiment descried in Section 3.3.2 show a strong linear relationship between number of printed layers and final height of printed objects. The average dry layer height is 2.18mm. This insightful result allows us to compensate for shrinkage in height of objects by suitably adding more layers thereby producing more accurate prints.

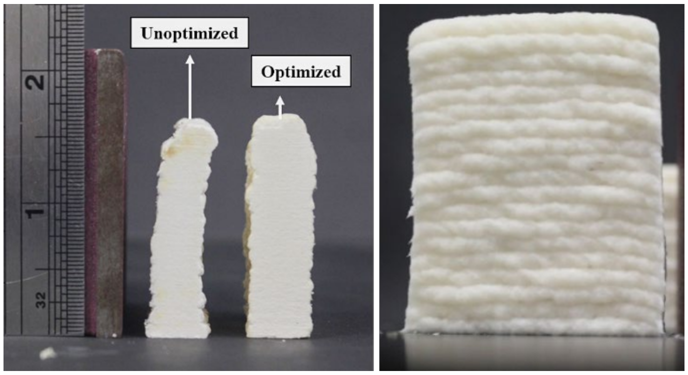

FIGURE 21. (LEFT) NEAR ELIMINATION OF CROSS-SECTIONAL TAPERING AS A RESULT OF OPTIMIZED INTER-LAYER SPACING. (RIGHT) SIDE VIEW OF OPTIMIZED WALL SHOWING CONSISTENT HEIGHT OF LAYERS

4.4 Large-Scale Printing with Results

The various insights garnered from the experiments presented in this work were combined to formulate a strategy to define toolpaths and print large-scale objects such as a 1.2m long

Journal of Mechanical Design. Received June 29, 2018;
Accepted manuscript posted January 05, 2019. doi:10.1115/1.4042624
Copyright © 2019 by ASME

wind turbine blade [Figure 22(A)]. The blade which has a NACA Symmetric Airfoil profile, was to be printed in two halves and glued together with the same material. A thin layer of the material is then plastered on the outer surface and smoothened through sanding operations.

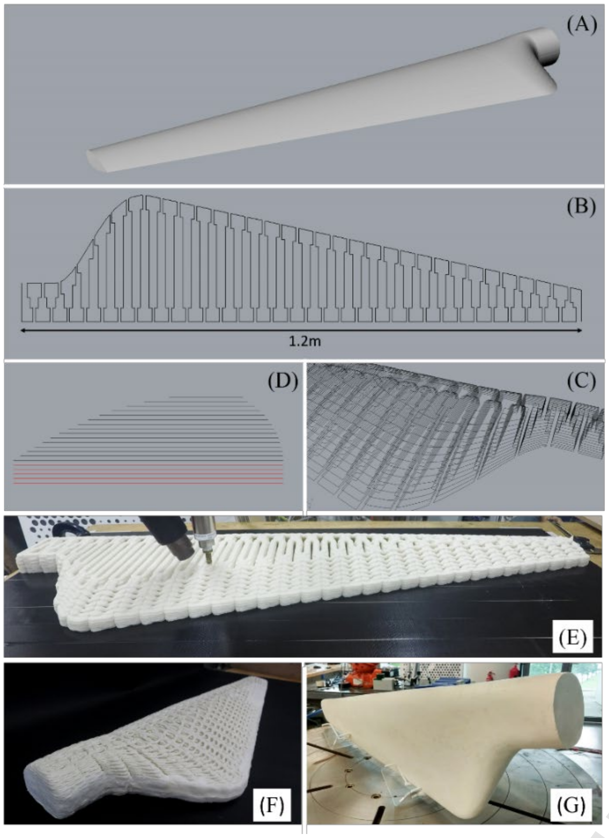

FIGURE 22. (A) WIND TURBINE BLADE DESIGN (B) TOP VIEW OF SERPENTINE PATH (C) PATH GENERATED FOR ENTIRE BLADE (D) EXTRA LAYERS (RED) FOR SHRINKAGE COMPENSATION (E) PRINTING ALONG GENERATED PATH (F) FUSED PRINTED HALVES (G) FINISHED TURBINE BLADE

The settings to print the blade were as obtained from the multi-objective optimization: $v_R = 49mm/s$, $z_N = 3.98mm$ and $f_M = 2.43ml/s$. These settings produce single filaments of width 12mm and height 4mm which were deemed suitable given the scale of the object. The pathing algorithm was generated based on results from the planar and vertical experiments performed. The object is first sliced into layers that are 3mm apart vertically to prevent tapering of cross-section of layers. To fill space within each layer, a serpentine pathing strategy was implemented which is algorithmically generated based on the boundary profile of the layer [Figure 22(B)]. The pattern consists of laterally overlapping units with voids in between, much like the square repeating patterns presented earlier. The length of the overlapping region and the overlap distance were set to 42mm and 6mm, as per results from Section 4.2, to ensure strong bonding between the units [Figure 22(C). Five additional layers spaced apart by 3mm each were added below the bottom most layer as seen in red in Figure 22(D) to compensate for shrinkage in height as per the trend observed in Figure 19. Given that the material shrinks more along its width (12%) than its length (5%), the direction of print was set to be perpendicular to the length of the blade. This configuration better preserves the cross-sectional shape of the blade given the smaller percentage of shrinkage along the length of filaments.

The encouraging results from printing of the blade in the very first attempt demonstrate the versatility and scalability of the developed process and print strategies. Other large-scale objects including a vertical single wall tubular structure of 0.25m height and 5m tall architectural structure (ongoing) were produced using the same print strategy [Figure 23].

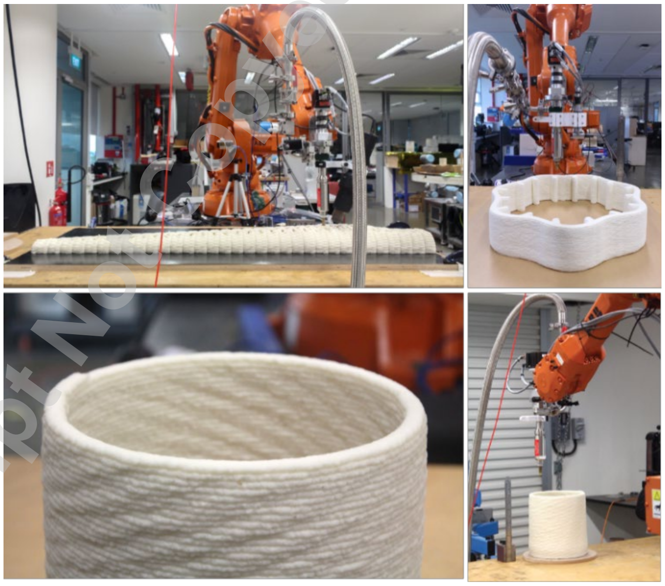

FIGURE 23. LARGE SCALE 3D PRINTED PROTOTYPES

5 CONCLUSIONS AND FUTURE WORK

The work presented here highlights facets from the development of a large-scale additive manufacturing process using sustainable natural composites. Through experiments, we developed the fundamental knowledge pertaining the interplay between the material and the extrusion process, relating controllable parameters to geometric and physical properties of individual filaments. We identified the lateral overlap settings that successfully fuse adjacent filaments with strengths greater than individual elements. We mitigated cross-sectional tapering of walls and showed linear scalability of shrinkage models in 3D space which can be used to preset toolpaths and allow for accurate prints. Combination of those results has enabled the successful production of large-scale prototypes. These endeavors reinforce the suitability of the methodical approach conducted in this study to achieve control of our additive manufacturing process with natural materials.

The presented parametrized approach is first step in a long path of process development and improvement opportunities. Exciting work lies ahead in evaluating the behavior of free-form

Journal of Mechanical Design. Received June 29, 2018;
Accepted manuscript posted January 05, 2019. doi:10.1115/1.4042624

designs and internal structural lattice patterns. The ability to systematically vary tensile properties of filaments during printing further opens an entire design space for producing functionally graded structures. While 3D printing with natural materials is certainly more challenging compared to well-behaved industrial grade material products, positive results towards understanding and controlling 3D printed biomaterials, positive steps towards this direction presented here, may impact general manifesting towards a more sustainable future.

6 ACKNOWLEDGMENTS

The authors would like to thank the SUTD-MIT International Design Center (IDC), SUTD Digital Manufacturing and Design Center (DManD) and National Additive Manufacturing Innovation Cluster (NAMIC) for supporting this project.

7 REFERENCES

[1] Duty, C. E., Kunc, V., Compton, B., Post, B., Erdman, D., Smith, R., Lind, R., Lloyd, P., and Love, L., 2017, "Structure and mechanical behavior of Big Area Additive Manufacturing (BAAM) materials," Rapid Prototyping Journal, 23(1), pp. 181-189.

[2] Wang, Z. Y., Liu, R. W., Sparks, T., and Liou, F., 2016, "Large-Scale Deposition System by an Industrial Robot (I): Design of Fused Pellet Modeling System and Extrusion Process Analysis," 3d Print Addit Manuf, 3(1), pp. 39-47.

[3] Barnett, E., and Gosselin, C., 2015, "Large-scale 3D printing with a cable-suspended robot," Additive Manufacturing, 7, pp. 27-44.

[4] Lee, J. C., Moon, J. H., Jeong, J.-H., Kim, M. Y., Kim, B. M., Choi, M.-C., Kim, J. R., and Ha, C.-S., 2016, "Biodegradability of poly(lactic acid) (PLA)/lactic acid (LA) blends using anaerobic digester sludge," Macromolecular Research, 24(8), pp. 741-747.

[5] Zia, K. M., Bhatti, H. N., and Ahmad Bhatti, I., 2007, "Methods for polyurethane and polyurethane composites, recycling and recovery: A review," Reactive and Functional Polymers, 67(8), pp. 675-692.

[6] Lim, S., Buswell, R. A., Le, T. T., Austin, S. A., Gibb, A. G. F., and Thorpe, T., 2012, "Developments in construction-scale additive manufacturing processes," Automation in Construction, 21, pp. 262-268.

[7] Perrot, A., Rangeard, D., and Courteille, E., 2018, "3D printing of earth-based materials: Processing aspects," Construction and Building Materials, 172, pp. 670-676.

[8] Brown, M. T., and Buranakarn, V., 2003, "Emergy indices and ratios for sustainable material cycles and recycle options," Resources, Conservation and Recycling, 38(1), pp. 1-22.

[9] Hajash, K., Sparrman, B., Guberan, C., Laucks, J., and Tibbits, S., 2017, "Large-Scale Rapid Liquid Printing," 3d Print Addit Manuf, 4(3), pp. 123-131.

[10] Gilberto, S., Dimitri, K., Rafael, L., K., H. M., Sydney, G. A., Antonia, N., Philippe, T., Tanja, Z., A., L. J., and R., S. A., 2017, "Cellulose Nanocrystal Inks for 3D Printing of Textured Cellular Architectures," Adv Funct Mater, 27(12), p. 1604619.

[11] Lam, C. X. F., Mo, X. M., Teoh, S. H., and Hutmacher, D. W., 2002, "Scaffold development using 3D printing with a starch-based polymer," Materials Science and Engineering: C, 20(1), pp. 49-56.

[12] Le Duigou, A., Castro, M., Bevan, R., and Martin, N., 2016, "3D printing of wood fibre biocomposites: From mechanical to actuation functionality," Materials & Design, 96, pp. 106-114.

[13] Li, V. C.-F., Dunn, C. K., Zhang, Z., Deng, Y., and Qi, H. J., 2017, "Direct Ink Write (DIW) 3D Printed Cellulose Nanocrystal Aerogel Structures," Scientific Reports, 7(1), p. 8018.

[14] Sanandiya, N. D., Vijay, Y., Dimopoulou, M., Dritsas, S., and Fernandez, J. G., 2018, "Large-scale additive manufacturing with bioinspired cellulosic materials," Scientific Reports, 8(1), p. 8642.

[15] ISO/ASTM52900-15, 2015, "Standard Terminology for Additive Manufacturing – General Principles – Terminology," ASTM International, West Conshohocken, PA.

[16] Lewis, J. A., 2006, "Direct ink writing of 3D functional materials," Adv Funct Mater, 16(17), pp. 2193-2204.

[17] Mogas-Soldevila, L., Duro-Royo, J., and Oxman, N., 2014, "Water-Based Robotic Fabrication: Large-Scale Additive Manufacturing of Functionally Graded Hydrogel Composites via Multichamber Extrusion," 3d Print Addit Manuf, 1(3), pp. 141-151.

[18] Fernandez, J. G., and Ingber, D. E., 2014, "Manufacturing of Large-Scale Functional Objects Using Biodegradable Chitosan Bioplastic," Macromol Mater Eng, 299(8), pp. 932-938.

[19] Suryakumar, S., Karunakaran, K. P., Bernard, A., Chandrasekhar, U., Raghavender, N., and Sharma, D., 2011, "Weld bead modeling and process optimization in Hybrid Layered Manufacturing," Computer-Aided Design, 43(4), pp. 331-344.

[20] Ding, D. H., Pan, Z. X., Cuiuri, D., Li, H. J., van Duin, S., and Larkin, N., 2016, "Bead modelling and implementation of adaptive MAT path in wire and arc additive manufacturing," Robotics and Computer-Integrated Manufacturing, 39, pp. 32-42.

[21] Rayegani, F., and Onwubolu, G. C., 2014, "Fused deposition modelling (FDM) process parameter prediction and optimization using group method for data handling (GMDH) and differential evolution (DE)," Int J Adv Manuf Tech, 73(1-4), pp. 509-519.

[22] Simunovic, S., Nycz, A., Noakes, M., Chin, C., and Oancea, V., 2017, Metal Big Area Additive Manufacturing: Process Modeling and Validation.

[23] Dritsas, S., "A Digital Design and Fabrication Library," Proc. Simulation in Architecture and Urban Design, Sprint Simulation Multiconference, SimAUD Group.

[24] Kalpakjian, S., 2010, Manufacturing engineering and technology, Prentice Hall, New York.

[25] Montgomery, D. C., 2012, Statistical Quality Control, 7th Edition, John Wiley & Sons.

[26] Kirk, R. E., 2015, "Experimental Design," The Blackwell Encyclopedia of Sociology.

[27] Seyed Shahabadi, S. M., and Reyhani, A., 2014, "Optimization of operating conditions in ultrafiltration process

Journal of Mechanical Design. Received June 29, 2018;
Accepted manuscript posted January 05, 2019. doi:10.1115/1.4042624

for produced water treatment via the full factorial design methodology," Separation and Purification Technology, 132, pp. 50-61.

[28] Trachtenberg, J. E., Placone, J. K., Smith, B. T., Piard, C. M., Santoro, M., Scott, D. W., Fisher, J. P., and Mikos, A. G., 2016, "Extrusion-Based 3D Printing of Poly(propylene fumarate) in a Full-Factorial Design," ACS Biomaterials Science & Engineering, 2(10), pp. 1771-1780.

[29] Morris, M. D., 1991, "Factorial Sampling Plans for Preliminary Computational Experiments," Technometrics, 33(2), pp. 161-174.

[30] Gunst, R. F., 1996, "Response Surface Methodology: Process and Product Optimization Using Designed Experiments," Technometrics, 38(3), pp. 284-286.

[31] Singh, S., Sharma, V. S., and Sachdeva, A., 2012, "Optimization and Analysis of Shrinkage in Selective Laser Sintered Polyamide Parts," Materials and Manufacturing Processes, 27(6), pp. 707-714.

[32] Vicente, G., Coteron, A., Martinez, M., and Aracil, J., 1998, "Application of the factorial design of experiments and response surface methodology to optimize biodiesel production," Industrial Crops and Products, 8(1), pp. 29-35.

[33] Dong, G., Wijaya, G., Tang, Y., and Zhao, Y. F., 2018, "Optimizing process parameters of fused deposition modeling by Taguchi method for the fabrication of lattice structures," Additive Manufacturing, 19, pp. 62-72.

[34] Derringer, G., and Suich, R., 1980, "Simultaneous Optimization of Several Response Variables," Journal of Quality Technology, 12(4), pp. 214-219.

[35] Ngo, T. D., Kashani, A., Imbalzano, G., Nguyen, K. T. Q., and Hui, D., 2018, "Additive manufacturing (3D printing): A review of materials, methods, applications and challenges," Composites Part B: Engineering, 143, pp. 172-196.

Journal of Mechanical Design. Received June 29, 2018;
Accepted manuscript posted January 05, 2019. doi:10.1115/1.4042624

ANNEX A

DISCUSSION ON RESIDUALS FROM DATA FITTING EXPERIMENT

It is important to individually examine the validity of fitted models by evaluating the assumptions made by the analysis of variance approach. ANOVA assumes that the model errors are 1) normally and 2) independently distributed with 3) same variance in each factor level. The model errors or 'residuals' are the differences between measured and fitted values at the various factor levels in the experiment. The Normal Probability Plot of the computed residuals allow evaluating the underlying assumption for error normality. Across the responses, the linearity of the Normal Probability Plots and associate histograms as seen in Figure 24 confirm the normality assumption of the residuals. The plots of Residuals against the Run Order for the responses lack any trends suggesting the runs were independent, free of experimental error and that the process is not influenced by any time dependencies. The third assumption can be verified by ensuring equal spread of residuals at each fitted value in the Residual vs Fitted Value plots. From the fitted models, a near equal spread of residuals is observed. The bias at certain values arises from the inherent nature of the Face-Centered design. As the design in non-rotatable [30] given that the axial runs are not at the same distance from the center of the design as the corner point runs in the experiment design space, we expect the standard deviation across fitted values to not be constant [25].

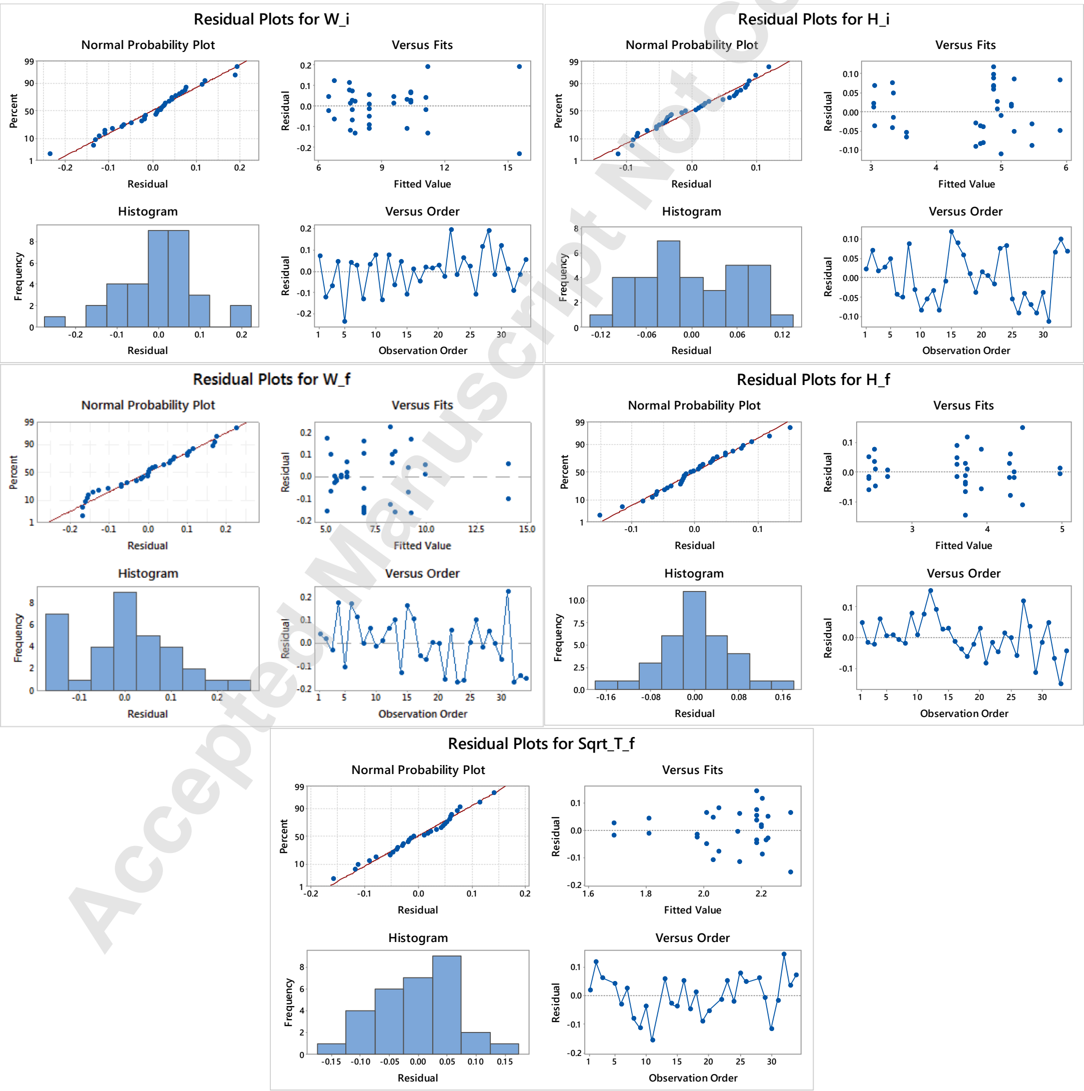

FIGURE 24. RESIUDAL PLOTS FOR FITTED MODEL

Journal of Mechanical Design. Received June 29, 2018;
Accepted manuscript posted January 05, 2019. doi:10.1115/1.4042624

List of Figures

List of Tables